Machine learning a bond order potential model to study thermal transport in WSe2 nanostructures

Machine learning a bond order potential model to study thermal transport in WSe$_2$ nanostructures

Henry Chan[1*], Kiran Sasikumar[1], Srilok Srinivasan[1], Mathew Cherukara[1],
Badri Narayanan[1,2], and Subramanian K. R. S. Sankaranarayanan[1,3*]

[1] Center for Nanoscale Materials, Argonne National Laboratory, Argonne IL, USA
[2] Department of Mechanical Engineering, University of Louisville, Louisville KY, USA
[3] Computation Institute, University of Chicago, Chicago IL, USA

Abstract

Nanostructures of transition metal di-chalcogenides (TMDC) exhibit exotic thermal, chemical and electronic properties, enabling diverse applications from thermoelectrics, catalysis to nanoelectronics. The thermal properties of these nanoscale TMDCs are of particular interest for thermoelectric applications. Thermal transport studies on nanotubes and nanoribbons remain intractable to first principles calculations whereas existing classical molecular models treat the two chalcogen layers in a monolayer with different atom types; this imposes serious limitations in studying multi-layered TMDCs and dynamical phenomena such as nucleation and growth. Here, we overcome these limitations using machine learning (ML) and introduce a bond order potential (BOP) trained against first principles training data to capture the structure, dynamics, and thermal transport properties of a model TMDC such as WSe$_2$. The training is done using a hierarchical objective genetic algorithm workflow to accurately describe the energetics, as well as thermal and mechanical properties of a free-standing sheet. As a representative case study, we perform molecular dynamics simulations using the ML-BOP model to study structure and temperature-dependent thermal conductivity of WSe$_2$ tubes and ribbons of different chiralities. We observe slightly higher thermal conductivities along the armchair direction than zigzag for WSe$_2$ monolayers but opposite for nanotubes, especially of smaller diameters. We trace the origin of these differences to the anisotropy in thermal transport and the restricted momentum selection rules for phonon-phonon Umpklapp scattering. The developed ML-BOP model is of broad interest and will facilitate studies on nucleation and growth of low

dimensional WSe$_2$ structures as well as their transport properties for thermoelectric and thermal management applications.

Corresponding Authors

*E-mail: hchan@anl.gov (H.C)
*E-mail: skrssank@anl.gov (S.K.R.S.S)

Introduction

The exotic thermal, chemical and electronic properties of transition metal di-chalcogenide (TMDC) nanostructures make them promising for wide range of technological applications[1, 2], including thermoelectrics, catalysis, and nanoelectronics. Among the TMDC monolayers, semiconducting WSe$_2$ has received a lot of attention for thermoelectric applications owing to its ultra-low thermal conductivity rivaling that of electrically insulating glasses[3, 4]. Recent works[3] indicate that intensive phonon localization in disordered WSe$_2$ can result in extremely low cross-plane thermal conductivity ($\sim 0.04 - 0.08$ Wm^{-1}K^{-1}) at room temperature. Shi and co-workers[5] experimentally demonstrated that thermal conductivity of disordered WSe$_2$ is six times lower than that of compacted single-crystal platelets. First-principles calculations suggest that the ultra-low thermal conductivity of WSe$_2$ monolayers (calculated values are 0.3 – 3.9 W/m.K depending on the sample size) can be attributed to the ultralow Debye frequency and high atomic masses of W and Se. Such low thermal conductivity of WSe$_2$ combined with its direct bandgap semiconducting nature make it promising for thermoelectric applications.

The thermoelectric efficiency of a material to convert heat into electricity (and vice versa) is measured by a figure-of-merit ZT defined as $ZT = \sigma S^2 T/\kappa$, where σ is electrical conductivity, S is Seebeck coefficient, κ is thermal conductivity and T is the absolute temperature[6, 7]. The thermal conductivity κ is the sum of phononic (κ_{ph}) and electronic (κ_e) contributions. Enhancement of the performance of a thermoelectric device, similar to other devices, entails developing materials with set of properties that often conflict with each other. An atomic-level understanding of both electron and phonon transport in WSe$_2$ nanostructures is crucial to realize their full potential in thermoelectric applications.

While electronic properties of WSe_2 have received a lot of attention[8-11], studies that focus on phonon transport through WSe_2 nanostructures are relatively scarce. Similar to other TMDCs, WSe_2 exhibits three acoustic phonon modes, namely, out-of-plane acoustic (ZA), transverse acoustic (TA) and longitudinal acoustic (LA) phonons[12]. A clear understanding of the relative contribution of each of these modes to overall thermal conductivity is vital for modulating heat transport in WSe_2 nanostructures, but remains elusive for finite size samples such as nanoscale ribbons. One of the major challenges in attaining such fundamental knowledge is the high computational expense of first-principles calculations leading to limitations in accessible length (supercell size < 1000 atoms) and time scales (~ 100 ps)[13-15]. Although the phonon band structure calculations together with Landauer-type approach should suffice for understanding the contribution of acoustic modes in small periodic systems, such restrictions have made first-principles techniques impractical for modeling phonon transport in desirable nanostructure geometries, such as tubes, slightly disordered 2D sheets, and other low dimensional structures.

As aforementioned, *ab initio* MD calculations can provide higher accuracy, but they remain limited in the system sizes (~ 100s of atoms) and time scales (~ 100s of ps) that can be probed. Classical molecular dynamics (MD) using empirical interatomic potentials provide a viable alternative and can access the necessary length- and time- scales (tens of nanometers, tens of nanoseconds) needed to model thermal transport in TMDC nanostructures. These empirical potentials can also inherently capture the full anharmonicity in these systems[16]. Several previous works have reported success in employing equilibrium (EMD) and non-equilibrium (NEMD) molecular dynamic simulations to assess thermal conductivity of nanoscale structures. For instance, Cherukara *et al.* have studied the thermal conductivity of stanene in the arm-chair and zigzag directions using equilibrium molecular dynamics (EMD) simulations and linear response theory (Green–Kubo formalism). The thermal conductivity of stanene sheets was found to be substantially lower than other 2-D materials such as graphene owing to low phonon group velocities (softness) and high anharmonic response[16]. Likewise, NEMD simulations were performed by Hong *et al.*[17] to compute thermal conductivity (κ) of TMDCs such as monolayer $MoSe_2$. They find that the thermal conductivity of the monolayer $MoSe_2$ sheet is lower and about half that of the monolayer MoS_2 sheet in

both armchair and zigzag directions. Classical MD is therefore a powerful technique to evaluate the thermal properties of a wide variety of 2-D materials.

The predictive power of classical MD calculations relies heavily on the quality of the empirical potentials describing the atomic interactions. Typically, these potentials are trained to reproduce experimental values (or accurate first-principles predictions) of various relevant material properties, including lattice parameters, cohesive energies, elastic constants, surface energies, and phonon dispersion relations[16, 18-22]. While there have been attempts to develop potential models for performing classical MD simulations of TMDCs, such models are often limited in their flexibility to model multi-layered and nanoscale TMDC structures. For instance, a reactive potential (ReaxFF) has been developed for MoS_2 (a representative TMDC), which can accurately describe its thermodynamic and structural properties[23]. However, this model was not trained against phonon dispersions, restricting its suitability for studying thermal transport in MoS_2 nanostructures. Furthermore, ReaxFF potentials are expensive compared to other empirical potentials such as Tersoff, Stillinger-Weber, etc; this makes it challenging to use ReaxFF for large-scale MD simulations necessary to assess thermal transport behavior of nanostructures. Recently, ReaxFF potential has been employed to investigate the thermal conduction in polycrystalline MoS_2. However, it is important to note that the primary goal of this work was to evaluate the thermal contact conductance at grain boundaries[24], which is relatively simpler than obtaining the intrinsic size-independent thermal conductivity of 2D sheets or 1D nanotubes. On the other hand, the available inexpensive models for TMDCs, such as Stillinger-Weber, are trained to reproduce phonon properties of $MoSe_2$, MoS_2 [17, 25, 26], and WSe_2 [27]. However, they treat the two layers of S/Se atoms in a monolayer with separate atom types; this is a major drawback, since these potentials are not suitable to investigate other dynamical behavior in TMDCs, such as their growth on substrates. Inspired by the success of classical MD simulations in modeling phonon transport, and the promise of WSe_2 nanostructures for thermoelectric applications, we focus on developing an inexpensive machine learned bond order potential (ML-BOP) that can accurately describe the structure, thermodynamics, phonon-transport, mechanics, and growth dynamics of monolayers, multilayers, and nanostructures of WSe_2. Note that although the focus of the current work is

on WSe_2, the ML strategy described here can enable potential models for any TMDC that retain accuracy of first-principles calculations, while being four orders of magnitude cheaper computationally.

Here, we use machine learning to train a bond order potential model that describes the complex potential energy surface of WSe_2 as well as accurately captures its structural, elastic, and thermal transport properties. Bond order potential models possess a complex functional form (with tens of independent parameters); developing such models requires a systematic parameterization approach that can efficiently sample the high dimensional parameter space. To accomplish such sampling, we leverage supervised machine learning methods powered by a combination of global and local optimization methods. We employ genetic algorithms using hierarchical objectives for global optimization, and Simplex to search for local minima; this technique leads to an optimum set of independent set of bond order parameters for WSe_2, without the need for human intuition or traditional heuristics. Our ML-BOP model is trained rigorously against an extensive first-principles based data set that includes lattice parameters, cohesive energies, equations of state, elastic properties and phonon dispersion. Using such a large-dataset enables ML-BOP to accurately capture the energetics, structure, mechanics, and thermal transport behavior of a wide range of WSe_2 nanostructures containing varied atomic configurations. To demonstrate the capability of our newly developed ML-BOP model, we first perform NEMD to study thermal transport in WSe_2 nanostructures at different temperatures. The ML-BOP predicted thermal properties at room temperature are in good agreement with previous experiments and first-principles calculations, which underscores its predictive power. Furthermore, we investigate the structural stability and atomistic mechanisms of phonon transport in WSe_2 nanosheets and nanostructures of WSe_2.

Methods

Functional Form: Our ML-BOP model employs the Tersoff-Brenner formulation to describe the atomic interactions. In this formalism, the total potential energy V of the system consists of pairwise contributions

from repulsive $f_R(r_{ij})$ and attractive $f_A(r_{ij})$ interactions between each distinct atomic pair i-j at a distance r_{ij} from each other. V is written as:

$$V = \tfrac{1}{2}\Sigma_i \Sigma_{j \neq i} f_c(r_{ij})[f_R(r_{ij}) + b_{ij}f_A(r_{ij})] \, , \tag{1}$$

where $f_c(r_{ij})$ is the cut-off function that limits the range of interaction to nearest neighbors, and is given by:

$$f_C(r) = \begin{cases} 1 \, , & r < R - D \\ \tfrac{1}{2} - \tfrac{1}{2}\sin\left(\tfrac{\pi(r-R)}{2D}\right), & R - D \leq r < R + D \\ 0 \, , & r \geq R + D \end{cases} \, , \tag{2}$$

where R and D define the cut-off distance of the potential. The repulsive and attractive contributions to the bond energy of i-j pair decay exponentially with the separation distance r_{ij}, written as:

$$f_R(r) = Ae^{-\lambda_1 r} \, , \tag{3}$$

$$f_A(r) = -Be^{-\lambda_2 r} \, , \tag{4}$$

where A, B, λ_1, and λ_2 are related to the dimer strength and Pauling constant.[29,30] The term b_{ij} in Equation 1 describes the bond-order for a pair of atoms i-j, which describes the weakening of an i-j bond owing to the presence of the other bond i-k around atom i. This term explicitly accounts for angular interactions *via* Equations 5-7:

$$b_{ij} = \left(1 + \beta^n \zeta_{ij}^n\right)^{\frac{-1}{2n}} , \tag{5}$$

$$\zeta_{ij} = \sum_{k \neq i,j} f_c\left(r_{ik}\right) g_{ik}\left(\theta_{ijk}\right) e^{\left[\lambda_3^m \left(r_{ij} - r_{ik}\right)^m\right]} , \tag{6}$$

$$g\left(\theta_{ijk}\right) = \gamma_{ijk}\left(1 + \frac{c^2}{d^2} - \frac{c^2}{d^2 + \left(\cos\theta_{ijk} - h\right)^2}\right). \tag{7}$$

The parameters β, n, λ_3, γ, c, d, and h are adjustable, while $m = 1$ (can only be 1 or 3) defines the variants of the Tersoff potential in LAMMPS and is not optimized (kept constant). In all, we optimized 13 independent parameters (γ, λ_3, c, d, h, n, β, λ_2, B, R, D, λ_1, and A) for each pair of atom types.

Training Data Set: The Tersoff functional form described above is used to describe the interactions between W-W, Se-Se, and W-Se. The potential parameters for W-W are obtained from Ref. 28, which is fitted to bulk W properties. However, the structure of bulk Se involves two major interaction distances, which the Tersoff function form, being a first neighbor only potential, can only model one of them. Therefore, instead of bulk Se structures, our Se-Se potential parameters are fitted to density functional theory (DFT) predicted energies of stable selenium clusters (see Fig. 1). These predicted energies are within 1% of the target values. The cross-interaction parameters for W-Se are fitted to an *ab-initio* derived training set that included the equation of state, cohesive energy, lattice constants, and phonon dispersion of WSe_2, calculated using DFT. All DFT calculations in the training set were performed using the Vienna ab-initio simulation package (VASP)[34,35]. The projector augmented-wave (PAW) atom potentials supplied with VASP were used, which included all *d*-electrons. We employed the Perdew-Burke-Ernzerof (PBE)[36] generalized gradient approximation (GGA) functional to treat the exchange-correlation. All calculations were performed on a single primitive cell of WSe_2 using a 520-eV plane-wave cutoff. The Brillouin zone was sampled using a 24×24×1 Γ-centered Monkhorst-Pack grid. Atomic coordinates were relaxed using conjugate gradient minimization until the force components on each atom was smaller than 10^{-3} eV/Å. A vacuum of 20 Å was employed in the direction normal to the plane of the WSe_2 sheet to avoid spurious interaction between periodic images. Phonon properties of WSe_2 are calculated using a finite difference method as implemented in Phonopy package.[37] To evaluate the dynamical matrix, we employ a 6×6×1 supercell, and a 4×4×1 *k* point grid; prior to introducing atomic displacements, the monolayer structure is optimized until all the atomic forces are less than 10^{-4} eV/Å.

Besides the use of first principle training data, we also complement it by adding in temperature dependent stability as one of the fitting criteria. The idea is to run on-the-fly MD simulations during the fitting process to assess the stability of various structures at different target temperatures. This approach addresses the problem of overfitting to energy minimized configurations that commonly leads to well fitted energy predictions but a lack of stabilities in MD and also missing of temperature dependency for the

predicted properties. Using this approach, we obtain Se-Se potential parameters that correctly capture the dynamics and relative stabilities of small Se clusters. For example, the potential is able to model the cis-trans isomerism of Se_6 ring and the ring opening/closing of Se_3. Furthermore, our W-Se potential parameters stabilizes a WSe_2 monolayer at a wide range of temperatures without the need to use any angular constrains or multiple atom types for Se atoms in the top and bottom layers[17, 25-27] (common fixes in other potentials).

Hierarchical Objective Genetic Algorithm Optimization: We evaluate the quality of the parameter set based on a hierarchical objective function (Fig. 2). In the HOGA evolutionary scheme, we truncate the evaluation of a parameter set which leads to large errors in hierarchal property classes and assign it a penalty depending on the class it fails at. The selection of hierarchical classes is at the discretion of the user. Our chosen hierarchy of the property classes for the WSe_2 parameter optimization is listed in Table 2. The hierarchical approach accelerates the traditional evolutionary search by (*i*) more efficiently sampling the parameter landscape in a given generation, and (*ii*) overcomes the limitation of a single objective that relies on assigning arbitrary weights.

Given the objective function definition as described in Fig. 2, we apply a two-stage optimization technique to search for a suitable parameter set for WSe_2 in the multi-dimensional parameter space. We use the genetic algorithm[29] (GA) for global optimization and the Nelder-Mead Simplex algorithm[30] for local optimization. Within the HOGA workflow, we initiate the global optimization process with ten initial population of N_p random parameter sets. The objective value $\Delta^{(i)}$ for each of these parameter sets is evaluated based on the hierarchical classes and their convergence is checked. If the convergence criteria are not met, genetic operations (selection, cross-over, mutation, etc.) are performed to arrive at a new list of N_p parameter sets based on the old parameter sets having the lowest objective values. The selection operation creates a list of best parameter sets based on their objective values, which mimics the principle of "survival of the fittest" in evolution. The cross-over operation intermixes these parameter sets to generate new set of good candidates; this procedure is analogous to how good traits are passed from biological parents to their offspring. The mutation operation introduces sufficient diversity into the population thereby

avoiding pre-mature GA run convergence. This allows the population the opportunity to improve beyond those possible via inheriting traits from parent structures (crossover). We use the tournament selection without replacement as the selection operation, the simulated binary method as the crossover operation with an operation probability of 0.9, and a polynomial of order 20 for the mutation operation with an operation probability of 0.1. For each of the parameter set, the objective value is evaluated followed by test for convergence. This routine is iteratively performed until we converge to a decent set of parameters, which is then subject to local optimization.

We typically perform at least 20 GA runs simultaneously (up to a total of 100 runs) to effectively sample the objective landscape. Each GA run typically has a population size of 200 and run for about 100 generations. The global optimization stage typically returns a list of decent parameter sets which we further refine using local optimization techniques. We use the Nelder-Mead Simplex algorithm[30] for local optimization. Note that the Simplex algorithm requires only function evaluations, and does not require function derivatives to be evaluated during the optimization. For minimization, a simplex with $(N + 1)$ vertices is constructed for a function with N variables. At each iteration, a vertex with the highest value is replaced with another point. During iterations, simplex contracts on to the final minimum given a good initial guess. The GA optimized parameter sets serve as the initial guess for Simplex. Owing to its simplicity, Simplex is widely popular for local optimization than some of the other methods that use derivatives such as Levenberg-Marquardt (L-M). Also, the combination of GA and Simplex has proven to be successful in our previous studies[31] and hence was also utilized in the present study. In principle, one can use any combination of global optimization and local optimization to train classical potential models for MD simulations.

Machine learning workflow: In our workflow, minimization of the cost function is done *via* a series of regression *akin* to the least squares or linear regression informed from supervising learning (GA combined with Simplex). Genetic algorithm (GA) and Simplex are used to generate/select the candidates based on these regressions. The ML-training set is built from features extracted from DFT calculations, which

includes atomic coordinates (~3000 data points), energies (~29 data points), phonon dispersion curves (~460 data points), etc. These features (data points) are organized into groups based on a hierarchy of property classes in descending importance (Table 2). We next sample the parameter space using GA followed by Simplex to obtain (a) errors in predictions of individual properties, as compared to DFT values, and (b) time necessary to compute them. Using these data, we identify connections between prediction errors for different property classes (e.g., structure, elastic constants, phonon dispersion etc.). These connections help us classify property classes that are most important, i.e., errors in which are strongly correlated with errors in others but require short compute times. In our hierarchical scheme, such property classes are placed first in the order. Essentially, the importance of a property class dictates its position in the hierarchical order as shown in Table 2.

Each group has an objective function that minimizes the weighted sum of squares of errors of the model predictions and the targets. The minimization process proceeds in order, group-by-group, and can terminate at any point if the group convergence criterion is not met. The objective function of group i is given by:

$$\Delta_i = \sum_j w_j \left(V_j^{predicted} - V_j^{target} \right)^2$$

where $V_j^{predicted}$ is the (BOP) model prediction, V_j^{target} is the (DFT) target for data point j in the group, w_j is the weighting factor. The weighting factor is applicable only within a group (i.e., not across groups), For the selection of weights, one may consider the relative focus of different simultaneously evaluated observables within a group (e.g., minimized atomic coordinate vs. minimized energy). In most cases, the data points in each group are weighted equally (no bias for particular points). The clustering and ordering of groups within the hierarchy is the main determining factor for the quality of the model for the different target properties.

The use of hierarchy overcomes two main problems with optimization in a high dimensional space, namely (a) it circumvents the use of a single objective and hence the training of the parameter sets is unaffected by

the choice of the weights when multiple objectives are present (b) allows for faster convergence and better sampling by weeding out parameter sets that are unlikely to lead to good solutions. In other words, the hierarchical optimization avoids getting stuck in local minima and performs a more elaborate global search to identify the optimal parameter set for the chosen target objectives.

Furthermore, in a departure from conventional force-field fitting, it is worth noting that the training is traditionally only performed against energetics or ground state properties *i.e.* derived from first-principles calculations. Temperature dependent properties and "stability checks" are seldom performed as part of the training procedure in conventional fitting. Often, the parameters obtained from such training may fit well against target energetics, but fail during an actual MD simulation *i.e.* dynamics at finite temperatures are incorrect due to poor representation of temperature dependent structural stability. Root mean square deviation (RMSD) of atom positions after a short MD run at different temperatures provides a way to estimate this instability (as illustrated in Fig. 3). For parameter sets that yield high RMSD, the energy is not conserved when simulations are performed at finite temperatures. To avoid this, we depart from conventional force-field fitting and explicitly check for "temperature dependent stability" during the training process. Each evolving population of parameter set is used to perform an on-the-fly MD simulation at different temperatures and checked to ensure energy is conserved.

Furthermore, it is worth noting the procedure outlined above also helps in circumventing issues arising from overfitting *i.e.* parameter sets that may lead to good predictions of energy (e.g. cohesive energy) but perform poorly overall in other properties (e.g. phonon dispersion). Such over-fitting can lead to unrealistic imaginary modes in the phonon dispersion curve, while providing excellent prediction of energetics. These imaginary modes (with negative frequencies in phonon dispersion) represent modes of deformation, which when activated (e.g., *via* temperature) will result in structural instability, i.e., spontaneous collapse of the structure. For example, Fig. 4 shows one such parameter set that predicts energy within 0.3 eV of DFT value, but exhibits imaginary modes in phonon dispersion. Although, the energy prediction at absolute zero is excellent, the imaginary modes get activated during a MD simulation at finite

temperatures (even at room temperature). Consequently, the structure collapses (i.e., is unstable) at finite temperatures. To avoid this issue, we check for imaginary modes in phonon-dispersion and RMSD of atoms within short MD runs at finite temperatures for promising parameter sets. The predictions of final trained ML model compared to values in ML-training set are discussed in the next section. The final parameter set listed in Table 1 is chosen based on the performance in validation tests.

NEMD simulations of thermal conductivities: The system is first equilibrated under an NPT ensemble at the respective temperature and a pressure of 0 bar, using Nose Hoover thermostat and barostat, for 300 ps. The system is subsequently equilibrated under NVT ensemble for additional 200 ps before computing the thermal conductivity. The NEMD simulations to compute the thermal conductivities of the nanostructures are performed with the Muller-Plathe algorithm. Here the simulation domain is divided into bins along the direction of heat transfer and a temperature gradient is created by exchanging kinetic energy between two particles in different bins of the simulation box (source and sink) every N steps. We use N=1000. Typical values in literature range from 100-5000. For small temperature gradients, linear response should be observed when NEMD is performed on a sufficiently equilibrated system. If the observed temperature gradient is not linear, then the energy is being swapped too frequently. In such cases N should be increased. We confirm for our simulations with N=1000 that we are indeed in the linear response regime. The bin size in NEMD simulation is approximately 5 Å. More details about the Muller Plathe algorithm can be found in Ref [32]. Note that in the present simulations, long-range Coulomb interactions were not employed since W and Se do not carry any formal charges. The timestep of integration used in all the simulations is 0.5 fs.

Results and Discussion

We assess the accuracy of our ML-BOP potential model by comparing its predicted values for several structural and mechanical properties of WSe_2 with those obtained from first principles calculations, and previous experiments reported in the literature (Table 3). The stiffness constants are calculated using the second-order derivatives of the energy with respect to strain (see Topsakal *et al*.[32] for details). Evidently,

the predictions of our ML-BOP are in good agreement with our DFT calculations, as well as the values

reported previously in literature.

Fig. 5 shows that our newly developed ML-BOP model captures phonon dispersion relations and

density of states (DOS) in good agreement with DFT calculations. The newly developed ML-BOP captures

the frequencies of the various acoustic and optical modes, within ~ 10 cm^{-1} of those derived from DFT.

This clearly demonstrates the suitability of our model to describe vibration (phonon) modes and thermal

transport in WSe$_2$. Note that the model has more emphasis on lower energy (acoustic) modes since an

adequate representation of these modes is needed to capture the thermal properties within a classical MD

force-field. Hence, in our parameterization, we weigh the acoustic branches much more compared to the

optical branches; this is the reason why the errors in the optical branches are much larger (Fig. 5(a)). The

temperature-dependence of specific heat capacity C_V of WSe$_2$ is also accurately captured by ML-BOP (Fig.

5(b)). It is worth noting that the C_V reaches 90% of the classical limit at about 150 K, and therefore we do

not expect any significant errors at temperatures higher than 150 K due to the difference in classical and

quantum phonon populations. Additionally, ML-BOP also describes well the energy-strain relationships in

monolayer WSe$_2$ (Fig. 5(c)), making it suitable to investigate mechanical behavior. Furthermore, Fig. 5(d)

shows a snapshot of a WSe$_2$ monolayer equilibrated at 300 K using the optimized parameter set. Note that

only a single atom type is needed to describe Se atoms in both the top and bottom layers.

Next, we demonstrate the capability of our newly developed ML-BOP model by investigating the

thermal transport along the armchair and zigzag directions of WSe$_2$ monolayer using Müller-Plathe reverse

non-equilibrium molecular dynamics (RNEMD) simulations. [33]. RNEMD techniques to evaluate the

thermal conductivity (κ) of bulk systems are influenced by finite size effects[34, 35]. Thermal conductivity in

the limit of L $\rightarrow \infty$ (κ_∞), where L is length of the system, is determined by performing RNEMD simulations

for several different L and extrapolating the $1/\kappa$ vs. $1/L$ plot to $1/L = 0$. Fig. 6(a) shows the computed values

of κ_∞ along the armchair and zigzag direction of a monolayer WSe$_2$ as a function of temperature. The

decrease in thermal conductivity with temperature can be attributed to the increased Umklapp scattering of

phonons at higher temperatures which is also observed in other 2D materials [16]. We also computed the

cross-plane thermal conductivity across the WSe_2 layers (Fig. 6(b)). Similar to the in-plane thermal conductivity, the out-of-plane thermal conductivity also decreases with temperature due to increased Umklapp scattering. The low cross-plane thermal conductivity is consistent with experimental reports [3, 36, 37]. Also as expected, the thermal conductivity in the cross-plane direction is much lower than the in-plane direction, similar to other layered nanomaterials.

Interestingly, the in-plane thermal conductivity along the armchair direction is marginally higher than that in zigzag, with this anisotropy being more prominent at low temperatures. We see a modest temperature averaged anisotropy ratio (armchair/zigzag) of 1.48 ± 0.47 that is consistent with prior reports[4, 38] within the error of the method (see Table 4). Specifically, WSe_2 nanoribbons have been reported with armchair direction phonon thermal conductance exceeding that in zigzag by a factor of 1.6 at 300 K and ~2x at 100 K[4]. Other first principles-based studies on monolayer WSe_2 have reported an armchair:zigzag anisotropy of 1.35 at 300 K[38]. The authors in Ref. [38] treat this anisotropy as relatively modest and subsequently only report the average isotropic thermal conductivity at other temperatures.

In such 2D materials, there are two sources of anisotropy – boundary and intrinsic. For instance, anisotropic phonon transport along the zigzag (ZZ) and armchair (AC) lattice directions has been reported in graphene nanoribbons[39]. Such anisotropy is absent in monolayer graphene[40]. In these cases, the anisotropy arises from the differential strengths of boundary scattering at the ZZ and AC edges of the nanoribbon. Typically, ZZ edsges have specular scattering, while AC edges have angle-dependent scattering. Other layered nanomaterials, such as black phosphorus[41], have been reported to have an intrinsic anisotropy as well. Here, the anisotropy in thermal transport is caused by anisotropic phonon dispersion and scattering rate along the ZZ and AC directions[41]. To clearly elucidate the origin of the anisotropy in monolayer WSe_2, and verify that the observed results is not a size/boundary artifact of the NEMD simulation, we calculate the expected values directly from the phonon dispersion employing the relaxation time approximation. The results are summarized in Table 4. We see that within, our method error the NEMD anisotropy is comparable to anisotropy from intrinsic effects. Nevertheless, the anisotropy ratio is modest (1 – 1.5) and for most practical purposes, WSe_2 monolayer can be considered isotropic.

Within the relaxtion time approximation (RTA) the effective thermal conductivity can be written as

$$\kappa(T) = \sum_{\lambda} C_{\lambda}(T)\, v_{\lambda}^2\, \tau_{\lambda}(T) \tag{8}$$

Where $C_{\lambda}(T)$, v_{λ}, and $\tau_{\lambda}(T)$ are the heat capacity, group velocity and relaxation time of the phonon mode λ. When the temperature is much greater than the debye temperature, the phonon-phonon Umklapp scattering rate takes the form[42, 43]

$$\frac{1}{\tau_{\lambda}{}^U} = \frac{\gamma_{\lambda}^2 k_B T \omega_{\lambda}^2}{M v_{\lambda}^2 \omega_{D,\lambda}} \tag{9}$$

where γ_{λ} and ω_D are the gruneissen parameter and debye frequency, respectively. Since all the phonon modes are populated in classical MD simulations, we can assume a constant debye frequency for all the branches. Hence,

$$\kappa(T) \propto \sum_{\lambda} \frac{C_{\lambda} v_{\lambda}^2}{\gamma_{\lambda}^2 \omega_{\lambda}^2} T \tag{10}$$

The anisotropy in the terms $\sum_{\lambda}(C_{\lambda}v_{\lambda}{}^2)$ and $\sum_{\lambda}(C_{\lambda}v_{\lambda}{}^4 / \gamma_{\lambda}{}^2\omega_{\lambda}{}^2)$, computed from DFT and the parameterized Tersoff potential, are listed in Table 4 along with the anisotropy from NEMD. Both the DFT and Tersoff potential shows limited anisotropy. Moreover, the anisotropy predicted from NEMD agrees resonably with the anisotropy reported from calculations based on first-principles and phonon Boltzman transport equation[38]. We find that the in-plane thermal conductivity of monolayer WSe_2 at room temperature is 13.04 $\pm$ 4.48. Our calculated out-of-plane thermal conductivity ($\sim 0.34 \pm 0.02$) is in between that measured previously by time-domain thermoreflectance (TDTR) (Ref. 3) for disordered WSe_2 (0.04 - 0.08 W/mK) and single crystal WSe_2 (~ 1.4 W/mK). In general, the k_{∞} predicted using ML-BOP is within the range of previously reported theoretical and experimental values 0.05 – 3.9 W/mK[3, 38].

Next, we investigate the structural stability and thermal transport in WSe_2 nanotubes. WSe_2 nanotubes modeled using our ML-BOP potential maintain their structural integrity over the entire range of temperatures considered in this work. Fig. 7(h) shows the k_{∞} calculated using

RNEMD for armchair and zigzag tubes with different diamters as a function of temperatures. Unlike the WSe$_2$ monolayer, the k_∞ shows relatively weak temperature dependence which can be attributed to the intrinsic stress assosiated with differential bending of the atomic layers in WSe$_2$. Fig. 7(a-c) and 7(d-f) shows the color mapping of the atomic stress across the cross-section of the armchair and zigzag tubes respectively. The inner Se layer experiences a compressive stress whereas the W and outer Se layers suffer from a tensile stress. This atomic stress weakens with increase in tube diameter. The suppression of temperature dependance is also observed in the case of Stanene nanotubes[16]. We attribute the slightly higher thermal conductivity in smaller tubes to the restricted momemtum selection rules for phonon-phonon Umpklapp scattering. A similar behaviour has been reported for carbon nanotubes[44]. A more detailed investigation is required to understand the exact diameter dependence of thermal conductivity.

Conclusions

In summary, we employed supervised machine learning approach to develop a bond order potential for W-Se system that accurately describes the structure, energetics, mechanics, and thermal transport properties of WSe$_2$ nanostructures. Our newly developed ML-BOP is a nearest-neighbor potential that accounts for directional effects; unlike other SW models available in the literature, ML-BOP does not treat Se atoms of different layers in WSe$_2$ monolayer as different atom types. This makes ML-BOP capable of describing well the structure, energetics, mechanical properties, and thermal transport in monolayer, multi-layer, disordered, and other low-dimensional nanostructures of WSe$_2$. Using this newly developed ML-

BOP, we studied the thermal transport behavior in monolayer WSe2, and nanotubes. We find that ML-BOP predicts a limited in-plane anisotropy in thermal conductivity consistent with previous reports based on first-principle calculations [4, 38]. In other words, the dynamics within our ML-BOP model correspond to a comparable phonon-phonon Umklapp scattering rates along the armchair and zigzag directions at room temperature. The ability of ML-BOP to accurately describe different atomic environments and bond formation/breaking opens new avenues for characterizing mechanical behavior and thermal transport in WSe_2 nano-structures. In particular, we envisage the use of ML-BOP for understanding cracking of WSe_2 nanostructures, the effect of grain boundaries on thermal transport, and thermo-mechanical behavior of TDMC heterostructures. Additionally, ML-BOP will enable understanding of the atomic-scale processes governing growth of WSe_2, the impact of various process variables on final as-grown nanostructure, as well as mixed TMDC monolayers.

Fig. 1 (a-f) Example selenium structures (dimer, trimer, ring, etc) in the training dataset. The table shows energies of these structures obtained from first principle calculations (target) and from the ML-BOP potential (predicted). See Table 1 for the optimized force field parameters for Se.
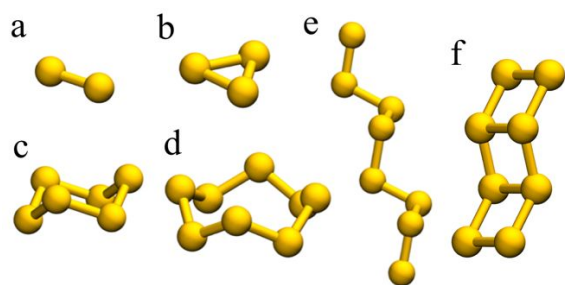
Energy (eV/atom)	**Target**	**Predicted**
a) Se_2	-2.030	-2.077
b) Se_3 (ring)	-2.170	-2.402
c) Se_6 (ring)	-2.522	-2.544
d) Se_8 (ring)	-2.585	-2.583
e) Se_8 (helix)	-2.380	-2.434
f) Se_8 (ladder)	-2.346	-2.397

Fig. 2 Supervised Machine learning workflow to train interatomic potential for WSe_2. The training set consists of heterogeneous data (energy, structure, phonon band structures, etc.) calculated from first principle methods and complemented by temperature dependent data from experiments. On-the-fly MD simulations are run during the fitting to assess the stability of various Se clusters and WSe_2 structures at their native temperature ranges. A hierarchical objective function is used to improve computational efficiency (early rejection) and to circumvent the need to assign arbitrary weights to the various properties in the heterogeneous data set (see Table 2 for the hierarchy of property classes). A two-stage approach is employed to navigate the high dimensional search space; evolutionary algorithm is used for global optimization, which is then followed by parameter refinements using local optimization (e.g., simplex) to obtained the optimized set of parameters. See table 1 for the optimized force field parameters for WSe_2.
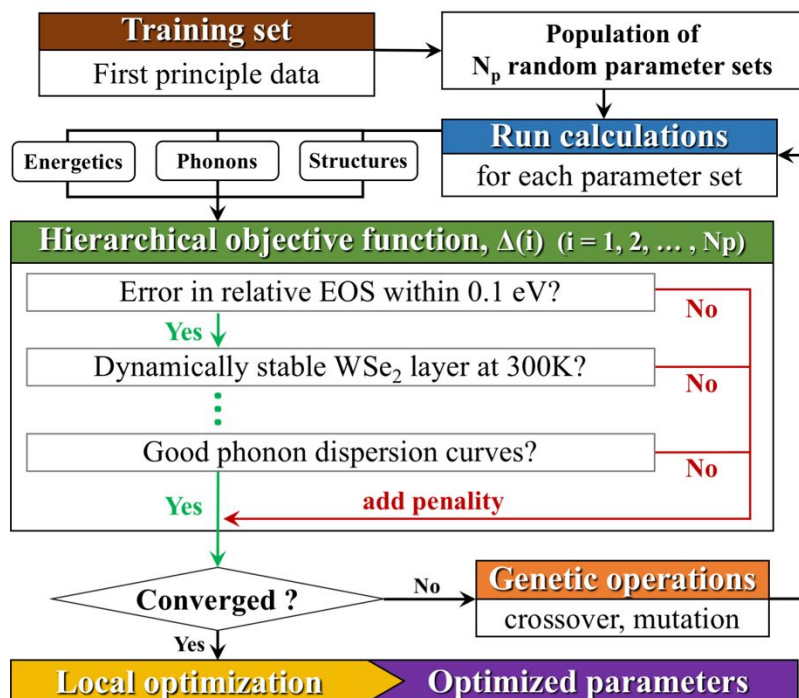
Fig. 3 Comparison of the predictions of the parameter sets evolving during the ML training. The parameter sets that poorly represent the temperature dependent structural stability are removed from the gene pool. Root mean square deviation (RMSD) of atom positions after a short MD run at different temperatures provides a way to estimate this instability and is used for updating the populations during the evolutionary optimization.
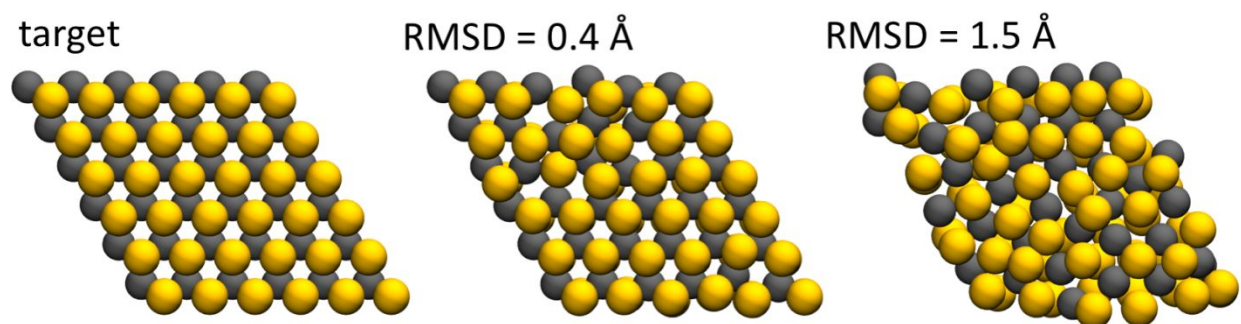
Fig. 4 Example of a parameter set that over-fits to cohesive energy. The predicted energy at T = 0 K is within 0.3 eV of DFT value, but the phonon dispersion exhibits unrealistic imaginary modes (negative frequencies). These frequencies represent modes of deformation that when activated at finite temperatures (even at room temperature) result in structural instability, i.e., spontaneous collapse of the structure in MD simulations.
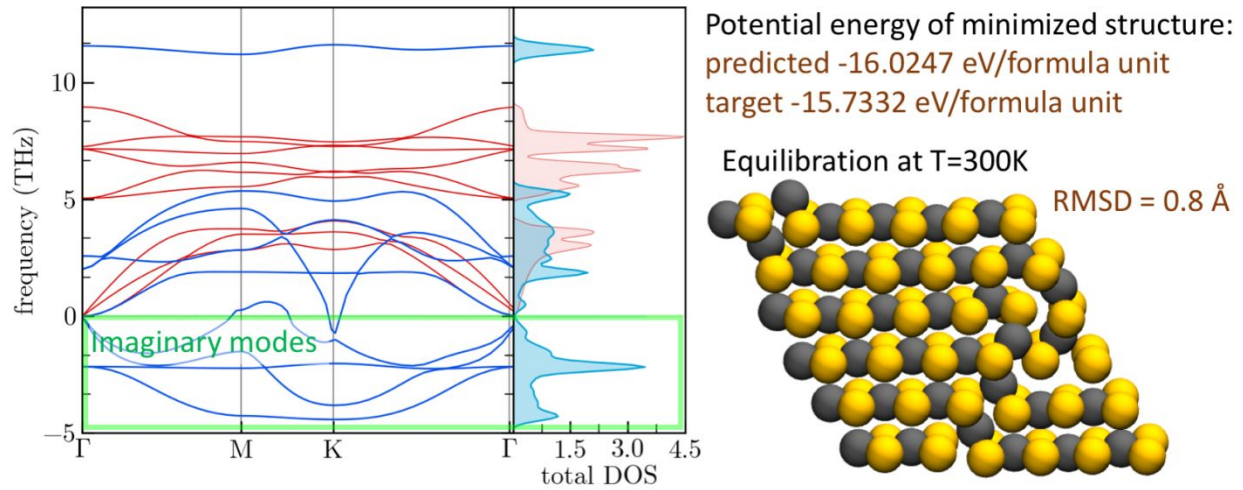
Fig. 5 (a) Comparison between ML-BOP (blue) and DFT (red) predicted phonon band structures and the total density of state. (b) ML-BOP and DFT predicted heat capacity as a function of temperature based on the quasi-harmonic approximation[45]. (c) ML-BOP and DFT predicted relative equation of state for a WSe2 monolayer (isotropic strain along in-plane directions). The two curves are vertically shifted with respect to their minimums for a clear comparison of their shapes. (d) Snapshot of a WSe_2 monolayer (periodic boundaries in the in-plane directions) equilibrated at 300 K. Se atoms in the top and bottom layers are represented by the same atom type. See table 1 for the optimized parameters.
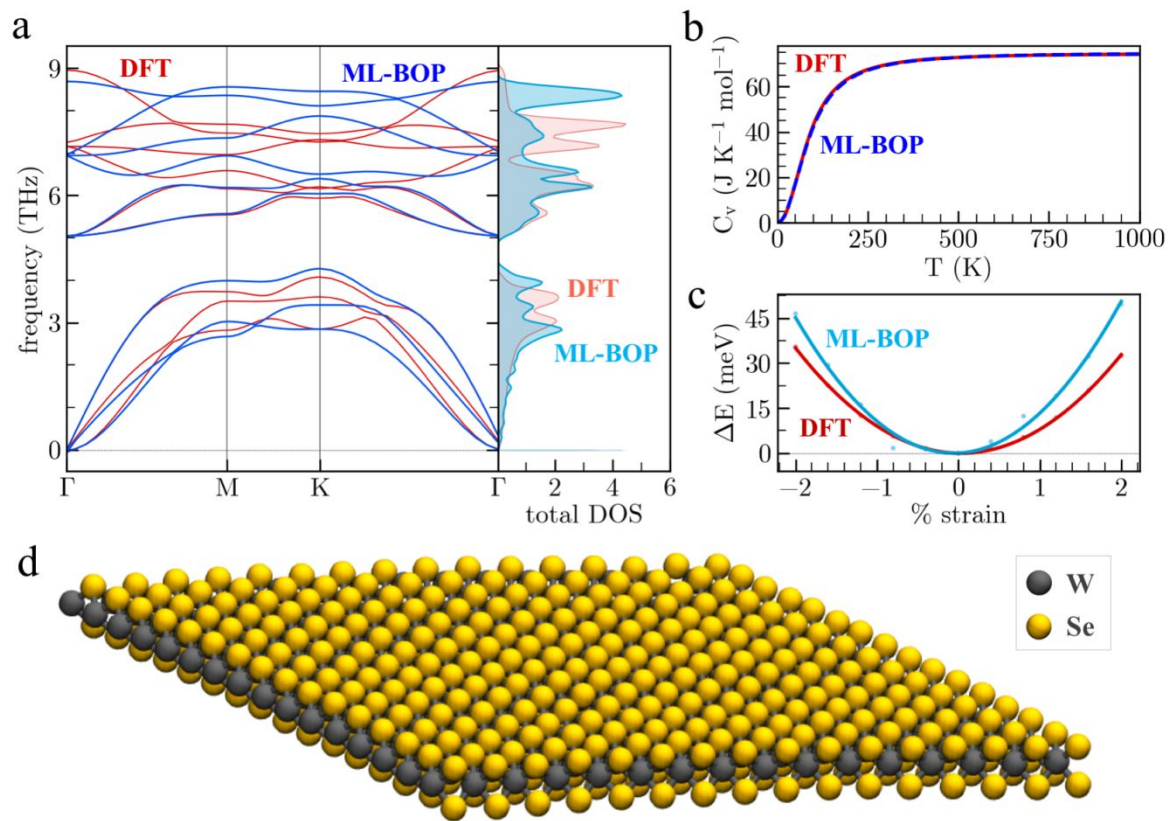
Fig. 6 (a) Thermal conducitivity along the armchair and zigzag direction of WSe$_2$ monolayers, (b) Thermal conductivity across the WSe$_2$ layers in the bulk.
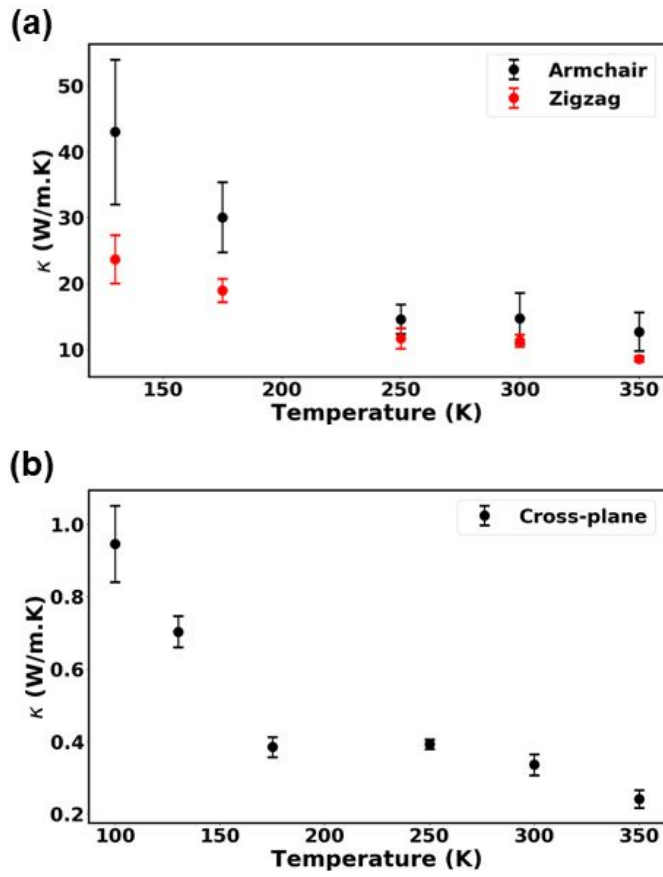
Fig. 7 Color mapping of atomic stress across the cross-section of (a-c) armchair tubes, (d-f) zigzag tubes and (g) along the axial direction of armchair tubes. Chirality of the tubes is listed in parentheses (in brown color). (h) thermal conductivity of nanotubes computed using RNEMD as a function of temperature.
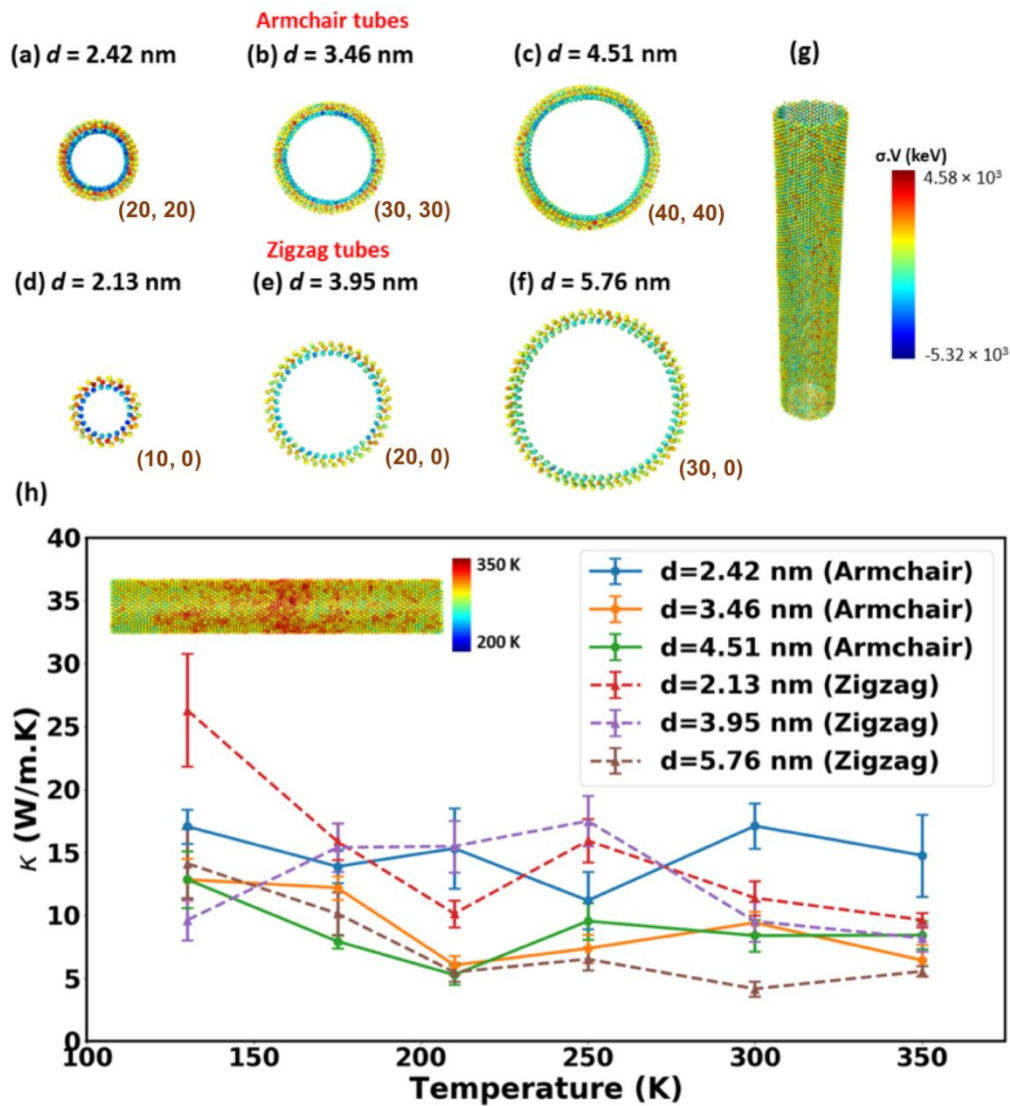
Table 1: Optimized ML-BOP force field parameters for WSe$_2$ obtained using our developed workflow. Parameters for W-W are obtained from Ref. 28.

	m	γ	λ_3 (Å^{-1})
W-W	1.0	0.00188227	0.45876
Se-Se	1.0	0.34906213	0.0
W-Se	1.0	1.83073272	-0.0021971

	c	d	h	n	β
W-W	2.14969	0.17126	0.2778	1.0	1.0
Se-Se	1.1986462544	1.06060163	-0.03966719	1.0	1.0
W-Se	1.3680636146	0.62917207	0.52270473	1.005583506	0.0792382146

	λ_2 (Å^{-1})	B (eV)	R (Å)	D (Å)	λ_1 (Å^{-1})	A (eV)
W-W	1.411246	306.49968	3.5	0.3	2.719584	3401.474424
Se-Se	1.958642032	880.03835004	3.41105925	0.37688017	2.937922484	4929.6960118
W-Se	1.349159955	175.93383819	3.26742071	0.76396915	3.214794733	4350.90479176

For Tersoff pair style in LAMMPS,

Element 1	Element 2	Element 3	Tersoff parameters
W	W	W	same as W-W
Se	Se	Se	same as Se-Se
W	Se	Se	same as W-Se
Se	Se	W	same as W-Se
W	W	Se	W-Se with $n = \beta = \lambda_2 = B = \lambda_1 = A = 0.0$
Se	Se	W	W-Se with $n = \beta = \lambda_2 = B = \lambda_1 = A = 0.0$
W	Se	W	W-W with $n = \beta = \lambda_2 = B = \lambda_1 = A = 0.0$
Se	W	Se	Se-Se with $n = \beta = \lambda_2 = B = \lambda_1 = A = 0.0$

Table 2: Hierarchy of the property classes used in HOGA optimization.

#	Hierarchy of property classes	Convergence Criteria
	For Se-Se,	
1	Minimized structure and energy of Se_2	RMSD < 0.02 Å, $|E_{predicted} - E_{DFT}|$ < 0.1 eV/atom
2	Shape of the Se_2 dissociation curve	average($|\Delta E|$) < 0.2 eV
2	Minimized structure and relative energy of Se_3 (ring)	RMSD < 0.05 Å, $|\Delta E_{predicted} - \Delta E_{DFT}|$ < 0.2 eV/atom
3	Minimized structure and relative energy of Se_6 (ring)	RMSD < 0.1 Å, $|\Delta E_{predicted} - \Delta E_{DFT}|$ < 0.05 eV/atom
4	Minimized structure and relative energy of Se_8 (ring)	RMSD < 0.1 Å, $|\Delta E_{predicted} - \Delta E_{DFT}|$ < 0.05 eV/atom
5	Minimized structure and relative energy of Se_8 (helix)	RMSD < 0.05 Å, $|\Delta E_{predicted} - \Delta E_{DFT}|$ < 0.05 eV/atom
6	Minimized structure and energy of Se_8 (ladder)	RMSD < 0.2 Å, $|\Delta E_{predicted} - \Delta E_{DFT}|$ < 0.2 eV/atom
7	Stability of Se_2	stable at T = 2273 K, dissociate at T = 3073 K
8	Stability of Se_6 (ring)	stable at T = 500 K, dissociate at T = 958 K
9	Stability of Se_8 (ring)	stable at T = 393 K, dissociate at T = 553 K
	For W-Se,	
1	Minimized structure and cohesive energy of WSe_2	RMSD < 0.02 Å , $|E_{predicted} - E_{DFT}|$ < 1.0 eV/atom
2	Equation of state	average($|\Delta E|$) < 0.005 eV
3	Phonon dispersion of WSe_2	no negative frequencies
4	Phonon dispersion of WSe_2	gamma point error < 0.4 THz
5	Phonon dispersion of WSe_2	band gap error < 0.2 THz
4	Phonon dispersion of WSe_2	minimize mean |error| of acoustic band frequencies
5	Phonon dispersion of WSe_2	minimize mean |error| of optical band frequencies
6	Stability of WSe_2 at T = 300 K, P = 1 bar	RMSD < 0.5 Å

Table 3: ML-BOP predicted properties for a WSe$_2$ monolayer compared to target values. Note that the values of elastic constants corresponding to shear modes of deformation show a higher deviation between DFT and classical calculation[46]. C$_{12}$ is one such shear constant and hence shows larger deviations from the target value.

	Predicted	Target (DFT)
lattice constant, a (Å)	3.350	3.327
C11 (GPa)	177.43	158
C12 (GPa)	76.57	31
C66 (GPa)	50.43	64
cohesive energy, E (eV)	-5.076	-4.517

Table 4: Anisotropies calculated from NEMD and RTA using the phonon frequencies from DFT and parameterized force field.

	Tersoff	DFT	Zhou et.al[38]
NEMD	1.48 ± 0.47	–	–
$\sum(C_v v^2)$	1.10	1.10	–
$\sum(C_v v^4 / \gamma^2 \omega^2)$	1.19	0.82	1.35

Conflicts of interest

There are no conflicts to declare.

Acknowledgements

References

1. X. Zhang, Z. Lai, Q. Ma and H. Zhang, *Chem. Soc. Rev.*, 2018, **47**, 3301-3338.

2. N. Choudhary, M. A. Islam, J. H. Kim, T.-J. Ko, A. Schropp, L. Hurtado, D. Weitzman, L. Zhai and Y. Jung, *Nano Today*, 2018, **19**, 16-40.

3. C. Chiritescu, D. G. Cahill, N. Nguyen, D. Johnson, A. Bodapati, P. Keblinski and P. Zschack, *Science*, 2007, **315**, 351-353.

4. J. Wang, F. Xie, X.-H. Cao, S.-C. An, W.-X. Zhou, L.-M. Tang and K.-Q. Chen, *Sci. Rep.*, 2017, **7**, 41418.

5. A. Mavrokefalos, N. T. Nguyen, M. T. Pettes, D. C. Johnson and L. Shi, *Appl. Phys. Lett.*, 2007, **91**, 171912.

6. G. J. Snyder and A. H. Snyder, *Energy Environ. Sci.*, 2017, **10**, 2280-2283.

7. H. J. Goldsmid, in *Introduction to thermoelectricity*, Springer, 2016, pp. 1-7.

8. W. Zhao, Z. Ghorannevis, L. Chu, M. Toh, C. Kloc, P.-H. Tan and G. Eda, *ACS Nano*, 2013, **7**, 791-797.

9. J. He, K. Hummer and C. Franchini, *Phys. Rev. B*, 2014, **89**, 075409.

10. P. Johari and V. B. Shenoy, *ACS Nano*, 2012, **6**, 5449-5456.

11. H. Sahin, S. Tongay, S. Horzum, W. Fan, J. Zhou, J. Li, J. Wu and F. M. Peeters, *Phys. Rev. B*, 2013, **87**, 165409.

12. Z. Jin, X. Li, J. T. Mullen and K. W. Kim, *Phys. Rev. B*, 2014, **90**, 045422.

13. T. K. Patra, F. Zhang, D. S. Schulman, H. Chan, M. J. Cherukara, M. Terrones, S. Das, B. Narayanan and S. K. R. S. Sankaranarayanan, *ACS Nano*, 2018, **12**, 8006-8016.

14. Z. Zhang, D. Schwanz, B. Narayanan, M. Kotiuga, J. A. Dura, M. Cherukara, H. Zhou, J. W. Freeland, J. Li, R. Sutarto, F. He, C. Wu, J. Zhu, Y. Sun, K. Ramadoss, S. S. Nonnenmann, N. Yu, R. Comin, K. M. Rabe, S. K. R. S. Sankaranarayanan and S. Ramanathan, *Nature*, 2017, **553**, 68.

15. Q. Pang, A. Shyamsunder, B. Narayanan, C. Y. Kwok, L. A. Curtiss and L. F. Nazar, *Nat. Energy*, 2018, **3**, 783-791.

16. M. J. Cherukara, B. Narayanan, A. Kinaci, K. Sasikumar, S. K. Gray, M. K. Y. Chan and S. K. R. S. Sankaranarayanan, *J. Phys. Chem. Lett.*, 2016, **7**, 3752-3759.

17. Y. Hong, J. Zhang and X. C. Zeng, *J. Phys. Chem. C*, 2016, **120**, 26067-26075.

18. F. G. Sen, A. Kinaci, B. Narayanan, S. K. Gray, M. J. Davis, S. K. Sankaranarayanan and M. Chan, *J. Mater. Chem. A*, 2015, **3**, 18970-18982.

19. B. Narayanan, K. Sasikumar, Z.-G. Mei, A. Kinaci, F. G. Sen, M. J. Davis, S. K. Gray, M. K. Chan and S. K. Sankaranarayanan, *J. Phys. Chem. C*, 2016, **120**, 17475-17483.

20. B. Narayanan, H. Chan, A. Kinaci, F. G. Sen, S. K. Gray, M. K. Y. Chan and S. K. R. S. Sankaranarayanan, *Nanoscale*, 2017, **9**, 18229-18239.

21. K. Sasikumar, B. Narayanan, M. Cherukara, A. Kinaci, F. G. Sen, S. K. Gray, M. K. Y. Chan and S. K. R. S. Sankaranarayanan, *Chem. Mater.*, 2017, **29**, 3603-3614.

22. M. J. Cherukara, B. Narayanan, H. Chan and S. K. R. S. Sankaranarayanan, *Nanoscale*, 2017, **9**, 10186-10192.

23. A. Ostadhossein, A. Rahnamoun, Y. Wang, P. Zhao, S. Zhang, V. H. Crespi and A. C. T. van Duin, *J. Phys. Chem. Lett.*, 2017, **8**, 631-640.

24. B. Mortazavi, R. Quey, A. Ostadhossein, A. Villani, N. Moulin, A. C. T. van Duin and T. Rabczuk, *Appl. Mater. Today*, 2017, **7**, 67-76.

25. A. Mobaraki, A. Kandemir, H. Yapicioglu, O. Gülseren and C. Sevik, *Comput. Mater. Sci.*, 2018, **144**, 92-98.

26. K. Ali, Y. Haluk, K. Alper, Ç. Tahir and S. Cem, *Nanotechnology*, 2016, **27**, 055703.

27. N. Payam and J. S. David, *Nanotechnology*, 2017, **28**, 075708.

28. N. Juslin, P. Erhart, P. Träskelin, J. Nord, K. O. E. Henriksson, K. Nordlund, E. Salonen and K. Albe, *J. Appl. Phys.*, 2005, **98**, 123520.

29. M. Mitchell, *An introduction to genetic algorithms*, MIT Press, Cambridge, Mass., 1996.

30. J. A. Nelder and R. Mead, *Comput. J.*, 1965, **7**, 308-313.

31. H. Chan, B. Narayanan, M. J. Cherukara, F. G. Sen, K. Sasikumar, S. K. Gray, M. K. Y. Chan and S. K. R. S. Sankaranarayanan, *J. Phys. Chem. C*, 2019, **123**, 6941-6957.

32.   M. Topsakal, S. Cahangirov and S. Ciraci, *Appl. Phys. Lett.*, 2010, **96**, 091912.

33.   F. Müller-Plathe, *J. Chem. Phys.*, 1997, **106**, 6082-6085.

34.   H. B. G. Casimir, *Physica*, 1938, **5**, 495-500.

35.   P. K. Schelling, S. R. Phillpot and P. Keblinski, *Phys. Rev. B*, 2002, **65**, 144306.

36.   P. Jiang, X. Qian, X. Gu and R. Yang, *Adv. Mater.*, 2017, **29**, 1701068.

37.   X. Qian, P. Jiang, P. Yu, X. Gu, Z. Liu and R. Yang, *Appl. Phys. Lett.*, 2018, **112**, 241901.

38.   W.-X. Zhou and K.-Q. Chen, *Sci. Rep.*, 2015, **5**, 15070.

39.   Z. Aksamija and I. Knezevic, *Appl. Phys. Lett.*, 2011, **98**, 141919.

40.   D. L. Nika and A. A. Balandin, *J. Phys.: Condens. Matter*, 2012, **24**, 233203.

41.   S. Lee, F. Yang, J. Suh, S. Yang, Y. Lee, G. Li, H. Sung Choe, A. Suslu, Y. Chen, C. Ko, J. Park, K. Liu, J. Li, K. Hippalgaonkar, J. J. Urban, S. Tongay and J. Wu, *Nat. Commun.*, 2015, **6**, 8573.

42.   D. T. Morelli, J. P. Heremans and G. A. Slack, *Phys. Rev. B*, 2002, **66**, 195304.

43.   P. G. Klemens, *Theory of the A-Plane Thermal Conductivity of Graphite*, 2000.

44.   L. Lindsay, D. A. Broido and N. Mingo, *Phys. Rev. B*, 2010, **82**, 161402.

45.   J. J. Plata, P. Nath, D. Usanmaz, J. Carrete, C. Toher, M. Jong, M. Asta, M. Fornari, M. B. Nardelli and S. Curtarolo, *npj comput. mater.*, 2017, **3**, 45.

46.   B. Narayanan, A. C. T. van Duin, B. B. Kappes, I. E. Reimanis and C. V. Ciobanu, *Modelling Simul. Mater. Sci. Eng.*, 2011, **20**, 015002.